

<https://doi.org/10.1038/s43247-024-01868-9>

Impact of tropical cyclones and socioeconomic exposure on flood risk distribution in the Mekong Basin

Check for updates

Aifang Chen^{1,2}, Yadu Pokhrel³, Deliang Chen^{4,5}, Hao Huang², Zhijun Dai⁶, Bin He⁷, Jie Wang⁸, Jiaye Li¹, Hong Wang² & Junguo Liu^{9,10} ✉

Tropical cyclones have a big impact on flood risk, and understanding how their activity interacts with population exposure under climate change is critical. Here we investigate spatiotemporal changes in flood risk using numerical models together with historical observations and future projections of tropical cyclone tracks. We find that tropical cyclone-related flood risk shifts from the Mekong Delta to the eastern lower Mekong Basin, driven by the interaction between tropical cyclones and population exposure. Historically, extreme precipitation from tropical cyclones increased flood risk in about 14% and decreased in 7% of the basin. Future tropical cyclones may increase flood risk in about 7% and reduce in nearly 18% of the basin. Moreover, population exposure growth has historically increased flood risk in 3% of the basin and is projected to result in a 1% increase. These findings highlight the complex interactions of tropical cyclone hazards and socioeconomic factors influencing flood risk.

Tropical cyclones (TCs) are a leading cause of extreme floods due to the associated heavy precipitation they bring upon landfall^{1–3}. Numerous studies have investigated the impact of TCs on flood hazards across various scales, revealing increasing trends linked to the intensification of TCs in the recent past and predicted future^{4–6}. These studies primarily focus on the TC-induced flood hazards associated with extreme precipitation, discharge, and storm surges^{7–10}. However, the joint influence of TCs and socioeconomic dynamics on flood inundation risk, which is the most direct consequence of floods leading to loss of human life and financial damages, remains elusive^{11–14}.

The rapid pace of socioeconomic development has significantly reshaped exposure to flood hazards and is considered a driving factor of flood risk worldwide^{15–18}. Studies quantifying socioeconomic exposure and climate change often emphasize the increasing risk trends driven by the accumulation of hazards and exposure^{19–21}. However, considerable spatial disparities exist in this risk due to the pronounced heterogeneity in the occurrence of natural hazards and the rates and levels of socioeconomic changes from migration and urbanization^{11,22}. In regions experiencing

declining trends in natural hazard occurrence, such as the decreasing TC frequency in the southwestern Western North Pacific²³, the prevailing factors of natural hazard risk may be obscured by the coarse resolution of analysis, overlooking the scale and distribution of risks at a local level^{20,24}. Thus, quantifying the impact of changes in TC precipitation-induced flood inundation (TCPinund) and societal development on TC flood inundation risk is challenging and crucial, particularly in light of the changing climate. This understanding will also facilitate the implementation of targeted mitigation measures to enhance societal resilience^{17,25}.

The Lancang–Mekong River Basin (LMRB) is prone to TCs and has experienced a distinct spatial pattern of changing TC activity between its northern and southern regions (Fig. 1) due to northwestward-shifting TC tracks in the Western North Pacific^{26–28}. It is likely to face more intense TCs under current predicted patterns of climate change^{29,30}. Furthermore, the LMRB continues to be a flood risk hotspot and is expected to encounter heightened flood risks in the future, potentially leading to significant adverse socioeconomic impacts^{31–33}. Moreover, the changing regional demographics and emerging economy necessitate an enhanced understanding of

¹School of Environment and Civil Engineering, Dongguan University of Technology, Dongguan, China. ²School of Environmental Science and Engineering, Southern University of Science and Technology, Shenzhen, China. ³Department of Civil and Environmental Engineering, Michigan State University, East Lansing, MI, USA. ⁴Department of Earth System Science, Tsinghua University, Beijing, China. ⁵Department of Earth Sciences, University of Gothenburg, Gothenburg, Sweden. ⁶State Key Laboratory of Estuarine and Coastal Research, East China Normal University, Shanghai, China. ⁷State Key Laboratory of Earth Surface Processes and Resource Ecology, Faculty of Geographical Science, Beijing Normal University, Beijing, China. ⁸College of Earth and Environmental Sciences, Lanzhou University, Lanzhou, China. ⁹Henan Provincial Key Laboratory of Hydrosphere and Watershed Water Security, North China University of Water Resources and Electric Power, Zhengzhou, China. ¹⁰Yellow River Research Institute, North China University of Water Resources and Electric Power, Zhengzhou, China. ✉e-mail: junguo.liu@gmail.com

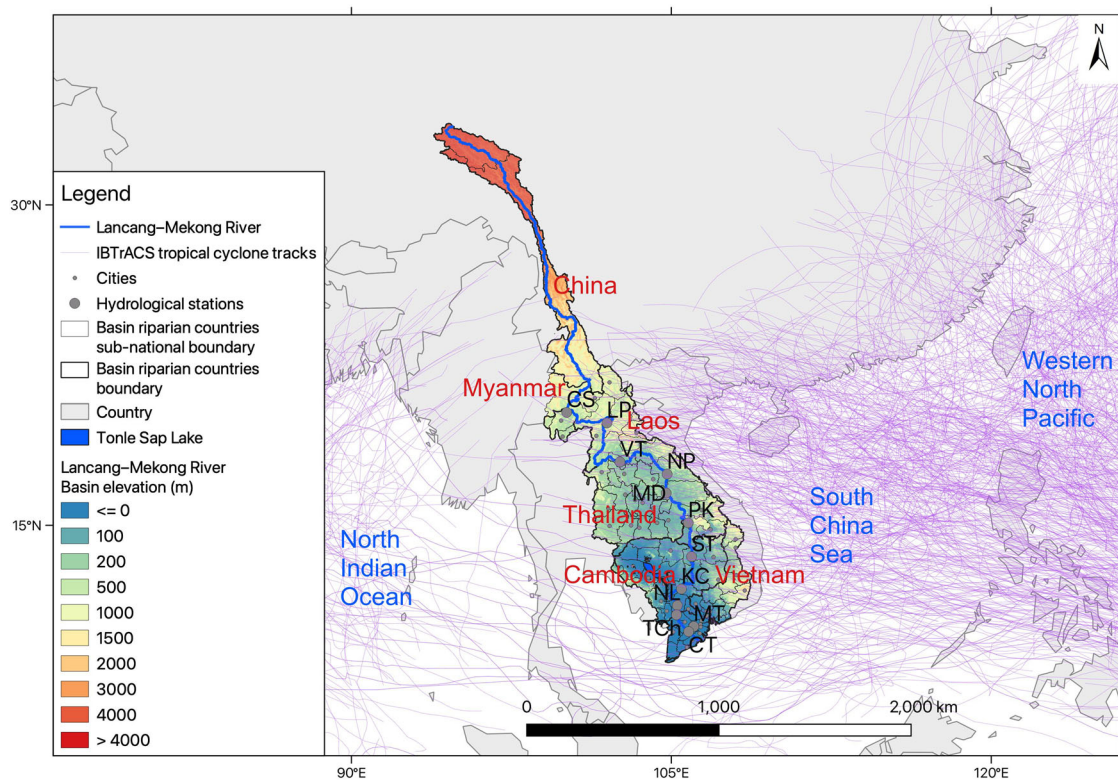


Fig. 1 | Location of tropical cyclone tracks and the Lancang–Mekong River Basin. Data sources: elevation data are from the Shuttle Radar Topographic Mission (SRTM) 90 m Digital Elevation Model (DEM) database. The Lancang–Mekong River and watershed data are from the HydroSHEDS database. Twelve

mainstream Lancang–Mekong River Basin stations are marked from upstream to downstream: Chiang Sean (CS), Luang Prabang (LP), Vientiane (VT), Nakhon Phanom (NP), Mukdahan (MD), Pakse (PK), Stung Treng (ST), Kompong Cham (KC), Neak Luong (NL), Tan Chau (TCh), My Thuan (MT), Can Tho (CT).

TCPinund for more effective regional flood risk management^{2,19–21,34}. Hence, it is imperative that we investigate the roles of changing TC activity and socioeconomic factors in past flood risk and estimate potential changes under future climate change.

This study addresses the following questions: (1) How is climate change altering the spatiotemporal dynamics of TCPinund in the LMRB? (2) What roles do TC activity and population exposure play in TCPinund risk? These questions are examined by employing the variable infiltration capacity (VIC) hydrological model³⁵ and the catchment-based macro-scale floodplain (CaMa-Flood) model³⁶ (hereafter referred to as the VIC-CaMa-Flood model). These models were used to simulate the daily flood inundation of TCs for the historical period 1967–2014, and projected future changes for the period 2027–2050 in the LMRB. TC tracks were obtained from the widely used observations of the latest available International Best Track Archive for Climate Stewardship (IBTrACS)³⁷ and modeling output of the TRACK algorithm from the Coupled Model Intercomparison Project Phase 6 High-Resolution Model Intercomparison Project (CMIP6 High-ResMIP) under high emission forcing³⁸. The VIC-CaMa-Flood model enables a physical processes-based investigation of precipitation- and non-TC precipitation-induced flood inundations over the LMRB domain, with satisfactory accuracy in simulating each inundation (see Supplementary Figs. 1 and 2), thus providing a significant advance in understanding changes in TCPinund.

To investigate changes in extreme TCPinund in the historical and future periods, we estimated the return period of TCPinund for 1967–1990, 1991–2014, and 2027–2050 based on the extreme value statistical model (see Methods)³⁹ at the grid scale. As we had only 24-year samples in each period, we estimated the 25-year return period of TCPinund in the historical periods (1967–1990 and 1991–2014) and the projection period (2027–2050) (abbreviated as $TCPinund25RL_{obs67-90}$, $TCPinund25RL_{obs91-14}$, and $TCPinund25RL_{mod27-50}$, respectively). Furthermore, we employed the

newly developed high-resolution global human settlement layer (GHSL R2023a) datasets on population density to assist in quantifying population exposure to TCPinund²⁴, thereby estimating flood inundation risk for the historical period (again split into 1967–1990 and 1991–2014) and the projection period (1991–2014 and 2027–2050) (abbreviated as $FloodRI_{obs67-90}$, $FloodRI_{obs91-14}$, $FloodRI_{mod91-14}$, and $FloodRI_{mod27-50}$, respectively). Finally, we examined the relative contributions of TCPinund and population exposure to flood inundation risk in each period. Our results showed that flood risk increased in significant parts of the basin from 1967 to 2014, while it is projected to be reduced in the Mekong Delta but increased in the lower eastern basin, influenced by changes in TC activity and population exposure.

Results

Changes in TC precipitation (TCP)

Primarily determined by the spatial pattern of TC tracks⁴⁰, annual daily extreme TCP during the historical period (1967–2014) and future projection period (2027–2050) significantly impacted most of the LMRB with pronounced “precipitation centers” located in the lower eastern portion of the basin (Fig. 2). Additionally, patterns of extreme TCP changed between the different periods studied. Compared with the period 1967–1990 (observation-based datasets, Fig. 2d), extreme TCP during 1991–2014 decreased within the “precipitation centers” of the lower eastern areas (south of 18° N). In contrast, the upper basin (north of 18° N) experienced an increase in extreme TCP. In the future projection for 2027–2050 (Fig. 2e), extreme TCP is expected to decrease in the lower eastern areas’ “precipitation centers.” Meanwhile, TCP in the central part of the upper basin is expected to decline, with small areas potentially experiencing increases compared to the period of 1991–2014. Additionally, the spatial pattern of TCP changes exhibited similarity to the annual TC occurrence (Supplementary Fig. 3). Thus, our results indicate declining trends in TCP in the

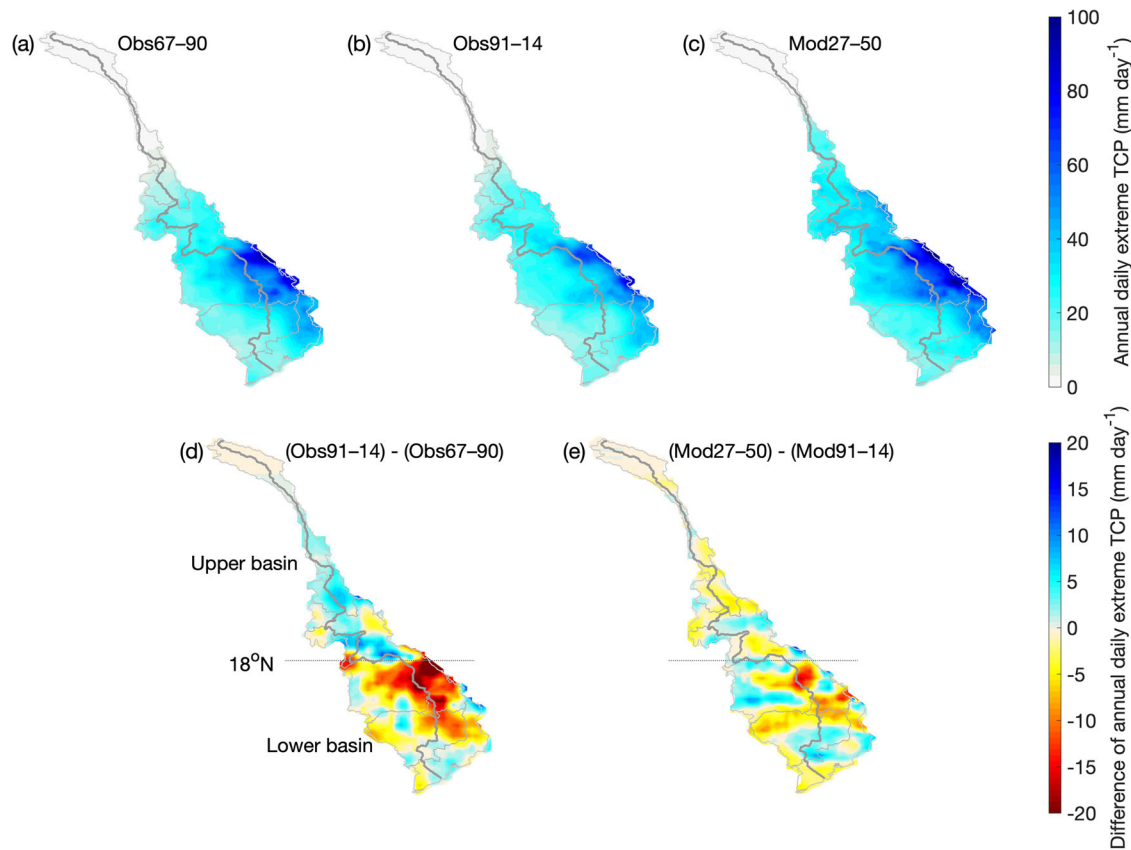


Fig. 2 | Spatial patterns of mean annual daily extreme tropical cyclone precipitation (TCP) and their difference between 1967–1990, 1991–2014, and 2027–2050. a, b Mean annual daily extreme TCP calculated using IBTrACS observation-based datasets in the historical periods 1967–1990 ($TCP_{obs67-90}$) and 1991–2014 ($TCP_{obs91-14}$), respectively. **c** Mean annual daily extreme TCP calculated

using HighResMIP model-based datasets in the future projection period 2027–2050 ($TCP_{mod27-50}$). **d** Difference between $TCP_{obs91-14}$ and $TCP_{obs67-90}$. **e** Difference between $TCP_{mod27-50}$ and the mean annual daily extreme TCP calculated using HighResMIP model-based datasets in the period 1991–2014 ($TCP_{mod91-14}$).

lower eastern parts of the LMRB during both historical and future periods, likely linked to changes in TC occurrence.

Changes in the 25-year return period of TCPinund

The spatial patterns of the mean annual extreme TCPinund showed similar patterns to those of extreme TCP (Supplementary Fig. 4). The “precipitation centers” in the lower eastern basin experienced high inundation during historical periods, while other areas experienced low inundation (Fig. 3a, b). Relative to $TCPinund25RL_{obs67-90}$, there was a substantial decrease in $TCPinund25RL_{obs91-14}$ in the lower western basin. However, increases were observed in the upper and lower eastern basins (Fig. 3c). The Mekong Delta exhibited a mixed pattern of increases and decreases in $TCPinund25RL_{obs}$ indicating a potentially divergent spatial flood pattern driven by TC activity in recent decades. Future projections of $TCPinund25RL_{mod}$ indicate that the central-eastern basin would face a higher risk of inundation (Fig. 3d, e). Compared with $TCPinund25RL_{mod91-14}$, the relative change in $TCPinund25RL_{mod27-50}$ suggests that the lower portion of the basin (south of 18° N) would experience a future increase in TCPinund, with the exception of the Mekong Delta (Fig. 3f). This is mostly consistent with the projected change in extreme TCP, inundation, and TC occurrence (Fig. 2, Supplementary Figs. 3 and 4). Meanwhile, the upper portion of the basin (north of 18° N) is projected to experience a decrease in inundation in the near future.

Changes in FloodRI

High FloodRI values were observed in most areas during the historical period (Fig. 4a–c), mirroring the spatial distributions of $TCPinund25RL_{obs}$ (Fig. 3a–c). A comparison of the $FloodRI_{obs}$ between the two historical periods (1991–2014 minus 1967–1990) indicated an

overall increased risk in the upper portion of the basin, the lower eastern basin, and parts of the Mekong Delta. Meanwhile, the lower western basin and most of the Mekong Delta exhibited a decreased risk. Changes in river tributaries exhibited a complex mixture of $FloodRI_{obs}$ with scattered positive and negative changes, especially in the lower western basin (Thailand). Compared with $FloodRI_{mod91-14}$, the future projection of $FloodRI_{mod27-50}$ depicted larger areas with reduced risk, while increased risk was prevalent in the lower eastern basin (Fig. 4d–f). Such a projection of future $FloodRI_{mod}$ is spatially consistent with the decreasing $TCPinund25RL_{mod}$ projection for 2030, except in the lower western basin and Mekong Delta. In summary, changes in FloodRI exhibited a regional shift of high risk from the Mekong Delta to the lower eastern part of the Mekong Basin in the future. Besides, the FloodRI presents more complex spatial patterns compared with those of TCPinund, suggesting a socio-economic role in reshaping flood inundation risk^{17,18,41}.

Furthermore, sub-national spatial distributions of population exposure showed distinct patterns, with high-risk concentration observed in specific provinces. Specifically, expressed proportionally, provinces near the Mekong Delta saw >40% of their provincial population exposed to $TCPinund25RL > 0.5$ m (representing moderate-to-high risk) (Fig. 5a, b). For moderate risk ($TCPinund25RL$ of 0.5–1 m, abbreviated as $TCPinund25RL_{mR}$), population exposure reduced during 1991–2014 compared to 1967–1990. However, high-risk ($TCPinund25RL > 1$ m, abbreviated as $TCPinund25RL_{hR}$) population exposure was more concentrated in provinces of the Mekong Delta (Fig. 5d, e). Meanwhile, comparisons showed a larger number of provinces with high risk than the moderate risk from 1967 to 2014. Exposure changes projected for 2027–2050 are expected to exacerbate moderate risk in the central and lower eastern basin and Mekong

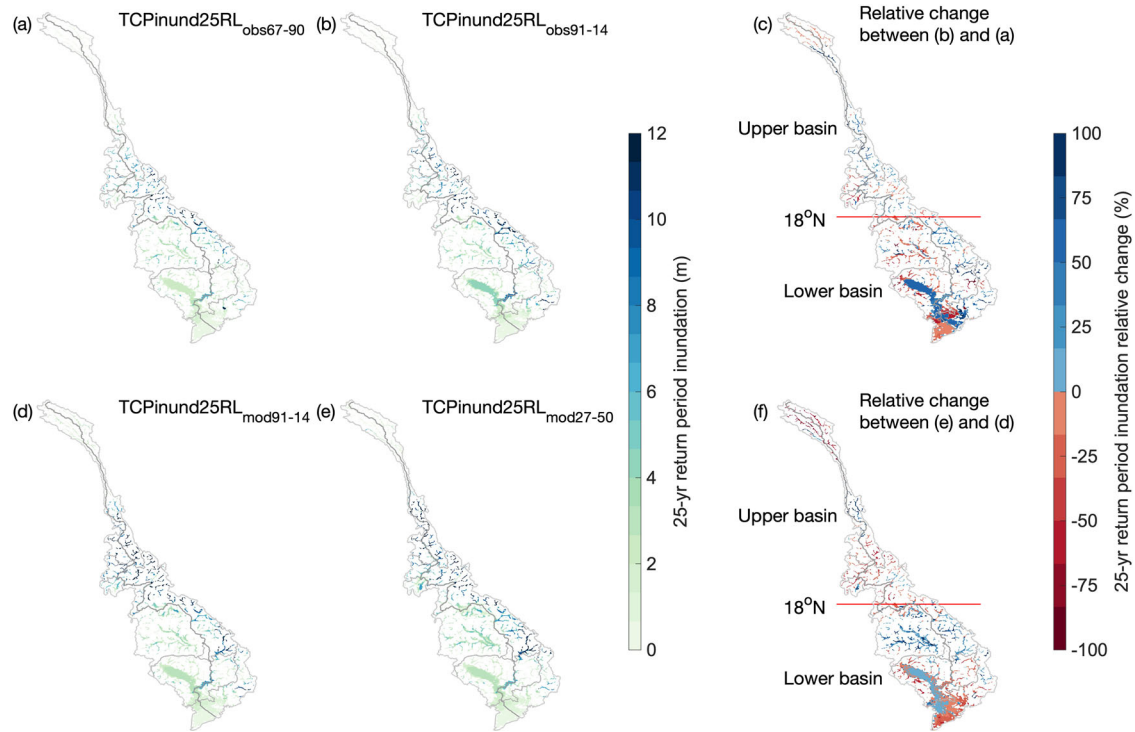


Fig. 3 | Spatial patterns of the 25-year return period of TCPinund (TCPinund25RL) and their difference between the historical and projected study periods. TCPinund25RL calculated from IBTrACS observation-based datasets (TCPinund25RL_{obs}) for the periods **a** 1967–1990 (TCPinund25RL_{obs67-90}) and **b** 1991–2014 (TCPinund25RL_{obs91-14}), along with **c** the relative change between the

two periods. TCPinund25RL calculated from the HighResMIP model-based datasets (TCPinund25RL_{mod}) for the periods **d** 1991–2014 (TCPinund25RL_{mod91-14}) and **e** 2027–2050 (TCPinund25RL_{mod27-50}), along with **f** the relative change between the two periods. All data are presented at a 5 km resolution for visualization.

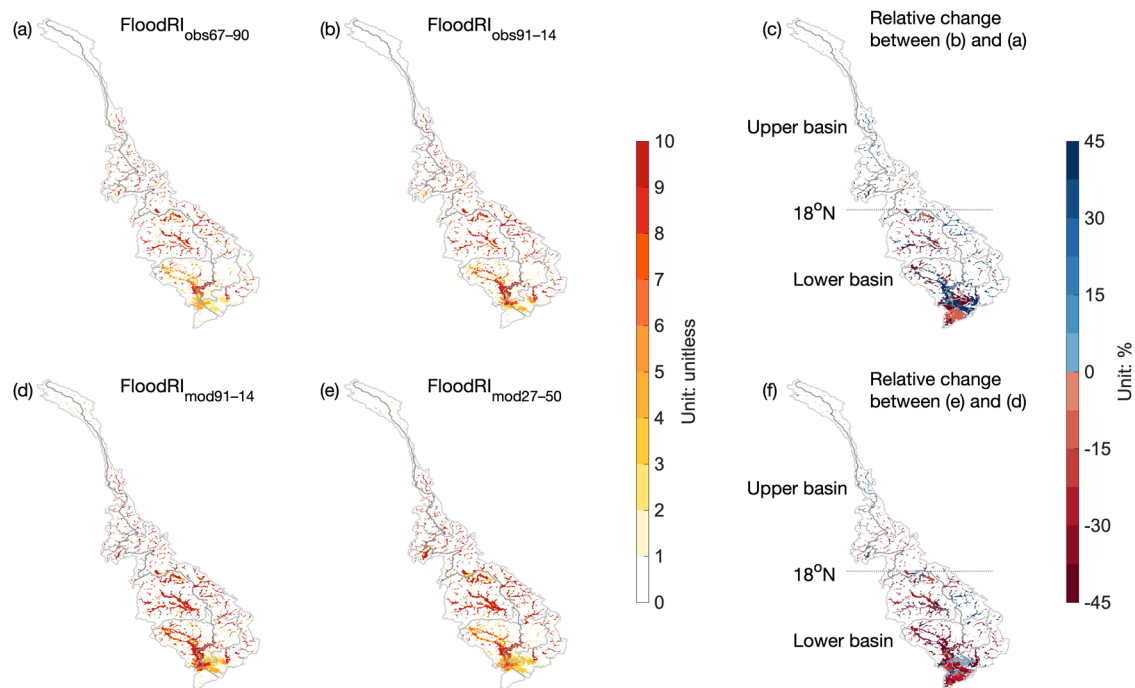


Fig. 4 | Spatial patterns of the FloodRI and their difference between the historical and projected study periods. FloodRI calculated from IBTrACS observation-based datasets (FloodRI_{obs}) during the periods **a** 1967–1990 (FloodRI_{obs67-90}) and **b** 1991–2014 (FloodRI_{obs91-14}), along with **c** the relative change between the two

periods. FloodRI calculated from HighResMIP model-based datasets (FloodRI_{mod}) during the periods **d** 1991–2014 (FloodRI_{mod91-14}) and **e** 2027–2050 (FloodRI_{mod27-50}), along with **f** the relative change between the two periods. All data are presented at a 5 km resolution for visualization.

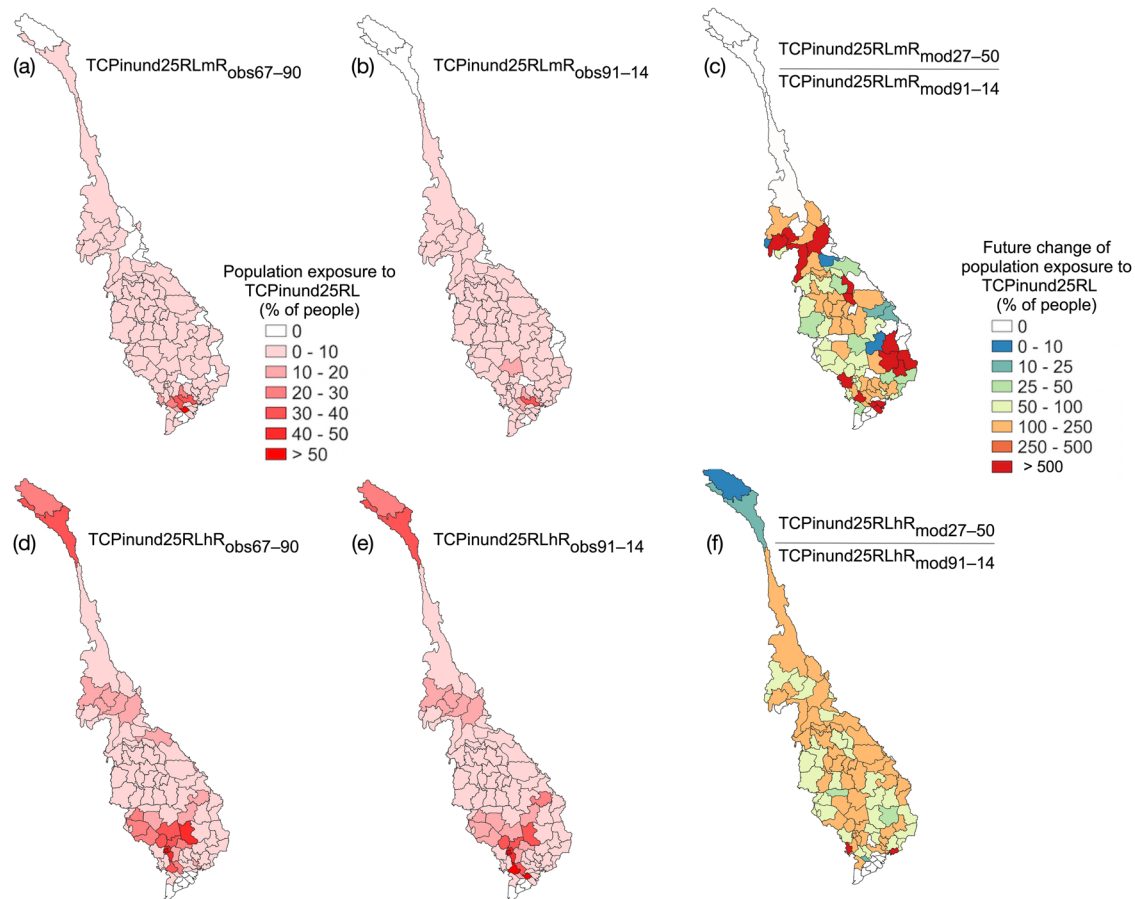


Fig. 5 | Sub-national regional maps showing spatial patterns of the proportion of the population exposed to the risk of TCPinund25RL during 1967–2050. TCPinund25RL a–c moderate risk (TCPinund25RLmR) and d–f high risk (TCPinund25RLhR). Population exposure to a, b moderate and d, e high risk of TCPinund25RL was calculated using the IBTrACS observation-based datasets during a, d 1967–1990 and b, e 1991–2014. c Relative change in exposure to TCPinund25RLmR of the HighResMIP model-based datasets between 1991 and

2014 and 2027–2050. f Relative change in exposure to TCPinund25RLhR of the HighResMIP model-based datasets between 1991–2014 and 2027–2050. Parts a and d are based on the population of 1990 exposed to TCPinund25RL risk during the period 1967–1990; parts b and e are based on the population of 2015 exposed to TCPinund25RL risk during 1991–2014; and parts c and f represent the potential change in the proportion of the population of 2030 exposed to TCPinund25RL risk during 2027–2050.

Delta. Furthermore, future projections generally indicate an aggravation of high-risk exposure across the basin. Overall, increases in TC-associated flood risk are projected to occur in provinces with high exposure (Fig. 5c, f, and Supplementary Fig. 5).

In addition, the list of the top ten sub-national administrative regions with the highest proportion of their population exposed to TCPinund25RL risk reveals provinces with notably elevated flood exposure, predominantly in Cambodia and Vietnam (Supplementary Table 1). From the past to the future, Phnom Penh in Cambodia remained at the top of high risk, and Vinh Long in Vietnam continued to rank at the top of moderate risk. Regarding the absolute exposed population, the list showed a slightly different picture (Supplementary Table 2). Regions with substantial TCPinund25RLhR flood exposure were mainly located in Vietnam, Cambodia, and China. Specifically, provincially, in the historical period, An Giang and Ho Chi Minh in Vietnam had the highest exposure to moderate and high risk, respectively. However, Ho Chi Minh and Phnom Penh are predicted to experience the highest risks in the future. These findings implied that provinces at the top of the lists (located proximately to the Mekong Delta) are focal points of TC-induced flood inundation risk in the LMRB.

Contributions of population exposure and TCPinund25RL to FloodRI

The relative contributions of exposure and natural hazards have revealed the driving factors behind the spatially divergent FloodRI (Fig. 6a, b). For the

entire LMRB domain, TCPinund25RL_{obs} led to increases in FloodRI_{obs} in 13.5% of the basin and decreases in 7.4% of the basin between 1991–2014 and 1967–1990 (Fig. 6e). When examining the upper and lower parts of the basin (with the dividing line at 18° N) separately, TCPinund25RL_{obs} caused increases in FloodRI_{obs} in more than 10% of both sub-basins. However, it led to larger decreases in FloodRI_{obs} in the lower basin (10.3%) than in the upper basin (2.5%), indicating a significant role for reduced TCPinund in lowering flood risk in the lower basin (Supplementary Fig. 6). Meanwhile, population exposure influenced FloodRI_{obs} across the entire domain (see Supplementary Fig. 5), resulting in an increase in FloodRI_{obs} in 3% of the domain and a decrease in 0.7% of the domain. At the sub-basin scale, population exposure led to increased FloodRI_{obs} in 2.7% of the upper and 3.2% of the lower basins. It had a lesser impact on decreasing FloodRI_{obs}, leading to decreases of 0.4% and 0.9% in the upper and lower basins, respectively. However, future changes in FloodRI_{mod} are projected to be dominated by changes in TCPinund_{mod} (Fig. 6b and Supplementary Fig. 6). Overall, results indicate that FloodRI_{mod} will decrease in most parts of the basin in the future, wherein TCPinund25RL_{mod} would contribute to increases in FloodRI_{mod} in 6.9% of the domain but decreases in FloodRI_{mod} in 18.1% of the domain. Despite this, the lower eastern basin and certain parts of the Mekong Delta will likely encounter increases in FloodRI_{mod}, dominated by increases in TCPinund. In addition, while the positive contribution of population exposure to FloodRI might shrink in the proportion of the domain to 1%, this could be attributed to population migration and more spatially

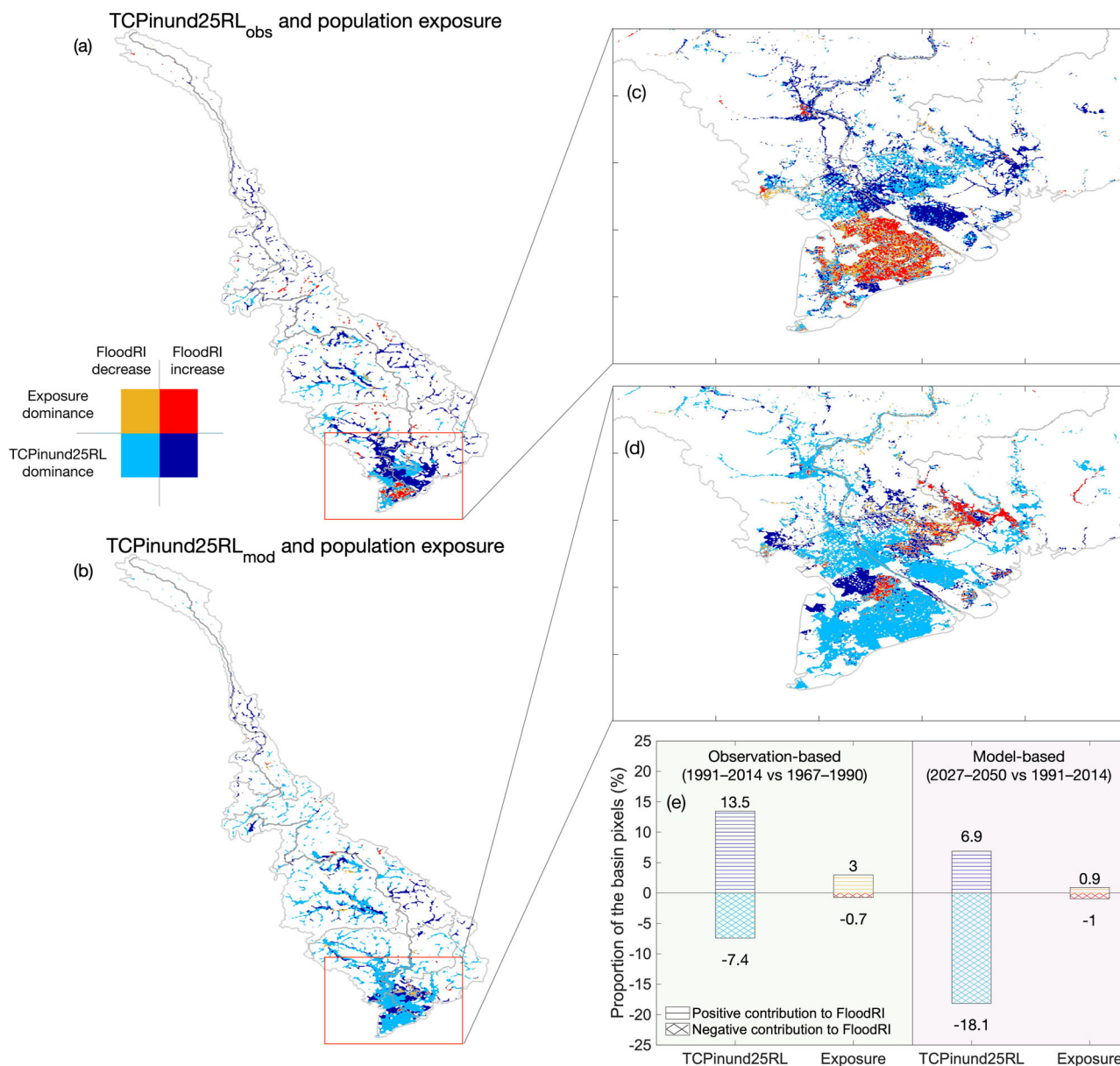


Fig. 6 | Spatial patterns of the relative contributions of the 25-year return period of TCPinund (TCPinund25RL) and population exposure to changes in the flood inundation risk index (FloodRI) in the LMRB during the periods 1967–1990, 1991–2014, and 2027–2050. Relative contributions to FloodRI calculated using IBTrACS observations (FloodRI_{obs}) during the historical periods 1967–1990 and 1991–2014 at 5 km resolution (a) and the zoom-in of Mekong Delta region at 1 km

resolution for visualization (c). Relative contributions to FloodRI calculated using HighResMIP modeling (FloodRI_{mod}) during the future periods 1991–2014 and 2027–2050 at 5 km resolution (b) and the zoom-in of Mekong Delta region at 1 km resolution for visualization (d). Statistical representation of the dominant proportional areas during the present and future periods (e).

aggregated urbanization, e.g., in Phnom Penh, Can Tho, and Ho Chi Minh City. Population exposure would also increase flood risk in the Mekong Delta (Fig. 6c, d). In conclusion, changes in FloodRI have been and will continue to be jointly influenced by natural hazards and exposure, with our findings indicating the reduced impact of TC activity on future flood inundation risk.

Discussion Impacts of TCs on flooding

Multiple factors can drive changes in flood risk. Numerous previous studies have investigated the risk associated with natural hazards^{31,42,43}. The effects of population exposure to floods, sea-level rise, and other natural hazards have been previously estimated^{16,17,44}. This study focuses on the changes in occurrence and population exposure to catastrophic TCs in the LMRB since the 1960s. By employing the VIC-CaMa-Flood hydrological-hydrodynamic

model, we assessed TC-associated flood inundation risk against the backdrop of shifting TC tracks in the Western North Pacific⁴⁵. Our results reveal that the spatially heterogeneous TC-induced flood inundation risk is linked to both the occurrence of hazards and population exposure. The extreme levels of TCPinund increased in the upper basin but decreased in the lower basin during 1991–2014 compared to 1967–1990. Meanwhile, future projections suggest a decrease in TC-induced flood inundation risk during the period 2027–2050 across significant portions of the basin, with TC-induced flood inundation hazards contributing to the declines in FloodRI in 10.5% of the upper basin and in 22.6% of the lower basin.

The activity of TCs is influenced by natural variability and global warming^{46,47}. Although future projections of the number of TCs are inconsistent^{48,49}, a northwestward shift of the TC track could result in a consistent reduction in the number of TCs hitting the LMRB. Our results showed a future decline in TC occurrence and extreme TCP in the lower

part of the basin (Fig. 2, Supplementary Fig. 3). However, this does not ensure a reduced flood risk in this region due to significant societal development. Areas undergoing population growth would generally experience an increase in TC-induced flood inundation risk, especially in flood-prone mega-cities experiencing rapid population growth. Overall, our findings indicate a regional shift of higher risk from the Mekong Delta to the lower eastern part of the Mekong Basin, driven by reduced TC tracks in the future compared to historical periods. Nevertheless, the Mekong Delta remains at risk.

Impacts of population exposure

Spatially disaggregating flood exposure highlights the most prevalent risks in the Mekong Delta within the LMRB. Despite a decrease in TCPinund25RL_{obs}, FloodRI_{obs} increased between 1967 and 2014, attributed to population exposure^{21,50}. Areas of increased FloodRI_{obs}, driven by population migration, were mainly observed in rapidly urbanizing major cities, leading to a more spatially aggregated pattern^{16,51}. In addition to this positive contribution, population migration negatively affects FloodRI, particularly in river tributaries. Specifically, the concentration of population exposure due to urbanization creates a socioeconomic pattern concentrated in a few administrative centers, resulting in a scattered distribution of both positive and negative FloodRI_{obs}. By 2030, as population exposure becomes more concentrated, it may reduce exposure in regions where people have moved out. However, it will also exacerbate exposure to TCPinund risk, especially in the TC flood-prone Mekong Delta.

Focusing solely on absolute exposure headcounts overlooks provinces with smaller populations but considerable relative exposure²⁰. Our result of sub-national exposure estimates presents different perspectives between absolute and relative terms (Supplementary Tables 1 and 2). Some provinces rank highly for population exposure in both absolute and relative terms, including Ho Chi Minh and Vinh Long in Vietnam and Phnom Penh in Cambodia, indicating high flood risks. Our results reveal increased anthropogenic pressures near rivers and coastal areas regarding flood risk⁵². As projected, the human population concentrated in low-elevation coastal zones (<10 m above sea level) globally will exceed one billion by 2060^{44,53}. Future socioeconomic growth may continue to elevate FloodRI, exacerbated by potential compound impacts of sea-level rise^{44,54} and land subsidence^{55,56}.

Existing studies generally highlight the contrast between economic flood exposure in developed countries and population flood exposure in developing countries^{11,20}. Here, we reveal population exposure risk occurring concurrently with rapid development in the LMRB, primarily concentrated in major cities of the Mekong Delta. Economic exposure in developing regions may be much less than in developed areas in absolute terms. However, such financial losses could still reverse years of progress in development and poverty reduction⁵⁷. Thus, our findings reveal a particularly concerning risk situation in developing countries.

Flood protection standards are crucial for flood protection⁵⁸, but these remain inadequate in the LMRB, leading to high levels of recent flood damage⁵⁹. A continuous increase in socioeconomic exposure may result in an exponential rise in catastrophic impacts, even for low-intensity hazards^{22,60}. Given that an aging population could exacerbate inequitable regional flood risk^{21,50,61,62}, regional development planning should consider exposure aggregation and decentralize population and economic activities away from flood-prone areas^{18,63,64}.

Conclusions

We have examined regional shifts in flood risk due to TC activity and population exposure in the TC-vulnerable LMRB using a hydrological-hydrodynamic model, historical observations, and future projections. Changes in TC precipitation led to increasing trends in extreme flood inundation in the lower eastern basin and parts of the Mekong Delta from 1967 to 2014. This trend is expected to continue, except in the lower western basin during 2027–2050, due to variations in TC occurrence and extreme TCP. A regional shift of higher risk of TC-induced flood inundation will likely occur from the Mekong Delta to the lower eastern basin in the future

compared to the historical period. The more complex spatial patterns of changes in the flood inundation risk index, compared to TC-induced flood inundation, highlight the significant role of population exposure in reshaping the risk. Nevertheless, the Mekong Delta is expected to remain the focal point of TC-related flood risk. Given the changing demographic landscape and inadequate flood protection measures, there is an urgent need for early plans to mitigate future TC risk by reducing socioeconomic exposure.

Methods

Data sources

The best track data of TCs from 1961 to 2014 was obtained from the latest IBTrACS version 4, which records TC tracks every three hours³⁷. A total of 309 TCs influenced the LMRB between 1967 and 2014. Daily water level data from 12 hydrological observation stations along the main stem of the LMRB from 1961 to 2014 was obtained from Mohammed et al.⁶⁵, Henck et al.⁶⁶, Annual Hydrological Reports of China, and the Mekong River Commission. Gridded daily precipitation data at a spatial resolution of 0.25° × 0.25° for 1961–2014 was obtained from APHRODITE v1101⁶⁷, known for its long-term and daily product for the LMRB with satisfactory accuracy⁶⁸. Other meteorological data (i.e., temperature and wind speed) from 1961 to 2014 was obtained from CN05.1⁶⁹ and the Princeton University Global Meteorological Forcing dataset⁷⁰.

For the analysis of future changes in TCs, we used TC track data from the CMIP6 HighResMIP calculated using the TRACK algorithm. This included historical simulation spanning 1967–2014 (highresSST-present) and future projection covering 2027–2050 (highresSST-future) from the CNRM-CM6-1-HR model, available at a spatial resolution of 25 km^{38,71}. The HighResMIP offers unique opportunities for future high-resolution TC track projection, and the 6-hour TC track from various HighResMIP models is freely accessible from the PRIMAVERA project. Among the available models of HighResMIP, CNRM-CM6-1-HR showed the highest accuracy in simulating TC tracks, providing data closest to the observations^{29,38,72}. For the simulation of model-based inundation, we used the TC track-associated meteorological variables (i.e., precipitation, temperature, and wind speed) from the corresponding CMIP6 CNRM-CM6-1-HR.

High-resolution grid population data was obtained from the open and freely accessible GHSL R2023a. These datasets provide spatial raster data between 1975 and 2020 in 5-year intervals, and projections to 2025 and 2030 derived from CIESIN GPWv4.11, with an available spatial resolution of 100 m; they have a satisfactory accuracy and have been employed to quantify population exposure in many studies^{18,24}.

Hydrological and hydrodynamic model

We used the VIC hydrological model (v4.20 d) and the CaMa-Flood hydrodynamic model (v3.6.2) to simulate TC-induced discharge and inundation in the LMRB. The VIC model is a widely used large-scale semi-distributed hydrological model applied in various river basins globally^{35,73}. The CaMa-Flood model is a global river hydrodynamic model known for explicitly parameterizing sub-grid-scale topography on floodplains^{36,74}. Here, the CaMa-Flood model was used to route input runoff simulated by the VIC model and describe the floodplain inundation dynamics of the lower LMRB. The flood depth was downscaled diagnostically to match the 500-m resolution Digital Elevation Model (DEM). The spin-up, calibration, and validation periods for the VIC-CaMa-Flood model were set to 1961–1966, 1967–1990, and 1992–2007, respectively. Due to the absence of a reservoir component in the VIC model for this study, simulations were not validated beyond 2007. For more details on model calibration, please refer to Wang et al.⁷⁵.

Comparisons of daily observed and simulated water levels showed that the VIC-CaMa-Flood model could effectively simulate water levels at hydrological stations from CS to TCh with small bias and relative error, and large Nash-Sutcliffe model efficiency coefficient (NSE) (Supplementary Table 3 and Supplementary Fig. 1). In contrast, performance was inadequate

at two stations near the river estuary (MT and CT) because of the unaccounted factors of the backwater effect of the tide and sand mining activities since the 1990s^{76–78}. In addition, the model captured interannual water level fluctuations at stations between CS and TCh exhibiting high Pearson correlation coefficients (see Supplementary Fig. 2 and Supplementary Table 4).

Simulation of TCPinund

We examined the impact of TCs on flood inundation by comparing the difference in simulation outcomes using precipitation forcings with and without TCP influence. Daily TCP was estimated as daily precipitation occurring within ±1 day when the TC center passed within a conventional threshold of a 500 km radius⁷⁹. Precipitation with the TCP influence was represented by daily precipitation (P, encompassing both TCP and nonTCP components), thereby influencing simulated inundation by both. Conversely, precipitation forcing without TCP was forced solely by daily nonTCP, obtained by excluding TCP from P, thereby simulating inundation influenced by other precipitation systems.

In simulating TCPinund for the historical period (1967–2014), we utilized TC track from the IBTrACS and precipitation data from APHRODITE (referred to as observation-based). For the simulation of TCPinund using HighResMIP climate models, TC track was taken from the HighResMIP calculated by the TRACK algorithm for both the historical period (1967–2014) and future period (2027–2050); precipitation was taken from CMIP6 CNRM-CM6-1-HR (referred to as model-based).

After obtaining the flood inundations caused by P and nonTCP from APHRODITE (abbreviated as Pinund_{obs} and nonTCPinund_{obs}, respectively), we constructed a 48-year climatology from 1967 to 2014 for both annual daily Pinund_{obs} and annual maximum daily Pinund_{obs} at each grid. Correspondingly, we constructed a 48-year climatology of the annual daily nonTCPinund_{obs} and annual maximum daily nonTCPinund_{obs} at each grid. To simulate the TCPinund based on HighResMIP modeling, we applied the widely adopted quantile delta mapping bias correction^{80,81} to the meteorological variables from CMIP6 CNRM-CM6-1-HR, using Eq. (1–3) with observational meteorological forcings. Subsequently, we derived Pinund_{mod} and nonTCPinund_{mod} simulated from the bias-corrected HighResMIP for both the periods 1967–2014 and 2027–2050.

To investigate the spatiotemporal influence of TCs on flood inundation, we estimated the trends of annual maximum daily precipitation and inundation of P, nonTCP, and TCP at the grid scale using Sen’s slope⁸² and the Mann-Kendall test⁸³. We then compared the correlation between changes in precipitation and inundation.

$$\widehat{x}_{m,r}(t) = F_{o,r}^{-1} \{ F_{m,r} [x_{m,r}(t)] \} \tag{1}$$

$$\Delta_m(t) = \begin{cases} \frac{x_{m,f}(t)}{F_{m,r}^{-1} \{ F_{m,f} [x_{m,f}(t)] \}} (\text{precipitation}) \\ x_{m,f}(t) - F_{m,r}^{-1} \{ F_{m,f} [x_{m,f}(t)] \} (\text{other meteorological variables}) \end{cases} \tag{2}$$

$$\widehat{x}_{m,f}(t) = \begin{cases} F_{o,r}^{-1} \{ F_{m,f} [x_{m,f}(t)] \} \Delta_m(t) (\text{precipitation}) \\ F_{o,r}^{-1} \{ F_{m,f} [x_{m,f}(t)] \} + \Delta_m(t) (\text{other meteorological variables}) \end{cases} \tag{3}$$

where, $F_{o,r}$, $F_{m,r}$, and $F_{m,f}$ are cumulative distribution functions of the daily meteorological variables of historical observations, historical modelings, and future projections, respectively; $x_{m,r}$ and $x_{m,f}$ are the daily meteorological variables of the historical modelings and future projections, respectively; and $\widehat{x}_{m,r}(t)$ and $\widehat{x}_{m,f}(t)$ are the bias-corrected daily meteorological variables of the historical modeling and future projections, respectively.

Estimation of TCPinund return period

We considered the spatially dependent patterns of TCPinund by employing an extreme value statistical model per grid-cell over the domain, which is particularly important in risk assessments^{84,85}. We

computed the TCPinund25RL for each grid cell by constructing empirical exceedance probability density functions for 1967–1990 and 1991–2014⁵. As we had only 24-year samples in each period, we estimated the return level of a 25-year return period, which was often practically relevant for flood planning and risk management. The non-parametric kernel density estimation function (Eq. (4)) was applied to any sample of flood inundation at a specific grid³⁹.

$$\hat{f}_h(f) = \frac{1}{nh} \sum_{i=1}^n K\left(\frac{f-f_i}{h}\right) \tag{4}$$

where, f_1, f_2, \dots, f_n are annual maximum daily simulations of TCPinund at each grid with unknown distribution; n is the sample size; K is the kernel smoothing function set as a normal kernel smoother; and h is the bandwidth set as 0.001 to provide sufficient detail for each kernel density estimation.

Next, we estimated the cumulative distribution function and exceedance probability function and obtained the return level estimate for each return period using a linear interpolation approach. The spatial distribution of the TC-induced inundation risk for the periods 1967–1990 and 1991–2014 was compared by using the difference between the respective TCPinund25RL values.

Future extreme TC-induced flood inundation with socio-economic projections

Given that the TC activity is expected to shift poleward under the currently predicted climate change patterns⁸⁶, the southern LMRB may continue to experience decreasing TC activity. Under this scenario, we estimated the projected TCPinund25RL for 2027–2050. We estimated the TC-induced flood inundations from the HighResMIP-based simulation (TCPinund25RL_{mod}) for the periods 1967–1990, 1991–2014, and 2027–2050 (abbreviated as TCPinund25RL_{mod67–90}, TCPinund25RL_{mod91–14}, and TCPinund25RL_{mod27–50}, respectively). Before analyzing future changes in TC-induced flood inundations, we compared the performance of TCPinund25RL_{mod} during 1967–1990 and 1991–2014 with that of TCPinund25RL_{obs}. Our results showed that TCPinund25RL_{mod} resembled the spatial distribution of TCPinund25RL_{obs}, but the model generally overestimated the absolute value of inundation (Supplementary Figs. 7 and 8). On this basis, we estimated the relative change in TC flood inundation depth ($\Delta TCPinund25RL_{mod}$) at both grid-scale and sub-national levels, using Eq. (5):

$$\Delta TCPinund25RL_{mod} = \frac{TCPinund25RL_{mod27-50} - TCPinund25RL_{mod91-14}}{TCPinund25RL_{mod91-14}} \tag{5}$$

Flood inundation risk index

To quantify societal exposure to extreme flood inundation, we estimated the FloodRI for the three study periods, using Eq. (6):

$$FloodRI = (\log_{10} Exposure) \times Hazard \tag{6}$$

where, *Hazard* is the TCPinund25RL (unit: m) and *Exposure* is the population density within the inundation zone (unit: number of people). For TCPinund25RL of 1967–1990, 1991–2014, and 2027–2050, we used population data from 1990, 2015, and 2030, respectively. In accordance with Zhu and Quiring⁵, we applied a logarithm of 10 transformations for *Exposure* to rescale the population for spatial analysis. The flood inundation risk index increases as the population density increases or TCPinund25RL becomes larger (higher physical TC flood inundation risk). We performed linear interpolation on the flood inundation data from 500 × 500 m to 100 × 100 m to align with the spatial resolution of the population data before computing FloodRI. The results were aggregated to a spatial resolution of 5 × 5 km to facilitate visualization.

Given the heterogenous TCPinund25RL and population density at the grid level, we applied a decomposition approach to examine the relative contribution of population exposure and TCPinund25RL to the anomaly of FloodRI (Eq. (7))⁸⁷. The respective contributions of population and TCPinund25RL were quantified as follows (Eq. (8)):

$$FloodRI' = ((\log_{10} Exposure) \times Hazard)' \quad (7)$$

$$\begin{cases} Con_{\log_{10} Exposure} = \frac{|\overline{Hazard} \times \log_{10} Exposure'|}{|\log_{10} Exposure \times Hazard'| + |\overline{Hazard} \times \log_{10} Exposure'|} \\ Con_{Hazard} = \frac{|\log_{10} Exposure \times Hazard'|}{|\log_{10} Exposure \times Hazard'| + |\overline{Hazard} \times \log_{10} Exposure'|} \end{cases} \quad (8)$$

where, $Con_{\log_{10} Exposure}$ and Con_{Hazard} represent the contributions of population exposure and TCPinund25RL, respectively; overbars and primes indicate the mean and its deviation, respectively.

In addition, we estimated the relative future change in FloodRI ($\Delta FloodRI_{mod}$) by comparing the relative changes between the periods 2027–2050 and 1991–2014, both at the grid-scale and sub-national levels, using Eq. (9):

$$\Delta FloodRI_{mod} = \frac{FloodRI_{mod27-50} - FloodRI_{mod91-14}}{FloodRI_{mod91-14}} \quad (9)$$

Exposure to significant TC-induced flood inundation risk at the sub-national level

To support regional flood risk management, we aggregated TCPinund25RL risk results at the sub-national level, offering a more straightforward comparison of flood risk among sub-nations. We first defined TCPinund25RL risk categories²⁰, assigning grid-level TCPinund25RL risk based on the following criteria: TCPinund25RL < 0.15 m = no risk (category 1); 0.15 m < TCPinund25RL < 0.5 m = low risk (category 2); 0.5 m < TCPinund25RL < 1 m = moderate risk (category 3); and TCPinund25RL > 1 m = high risk (category 4). Categories 3 and 4 represent areas with substantial TC-induced flood inundation risk. We used the category assignments to calculate the population exposed at the grid level, and then aggregated these results at the sub-national administrative level to derive absolute population exposure values. Additionally, we computed proportional population exposure by considering the total population of each sub-national unit. With these data, we investigated the spatiotemporal patterns of population exposure to TC-induced flood inundation risk.

Reporting summary

Further information on research design is available in the Nature Portfolio Reporting Summary linked to this article.

Data availability

The datasets presented in this study can be found in the latest International Best Track Archive for Climate Stewardship (<https://www.ncei.noaa.gov/data/international-best-track-archive-for-climate-stewardship-ibtracs/v04r00/access/netcdf/>) and Asian Precipitation-Highly-resolved Observational Data Integration Towards Evaluation (APHRODITE, https://search.diasjp.net/en/dataset/APHRO_MA) database. The TC tracks and associated meteorological data for the Coupled Model Intercomparison Project Phase 6 High-Resolution Model Intercomparison Project (CMIP6 High-ResMIP) models are available as a part of the PRIMAVERA project from the Centre for Environmental Data Analysis archive (<https://catalogue.ceda.ac.uk/uuid/0b42715a7a804290afa9b7e31f5d7753>). The newly developed high-resolution global human settlement layer (GHSL R2023a) datasets (<https://ghsl.jrc.ec.europa.eu/download.php?ds=pop>). Elevation data come from the SRTM 90 m DEM database (<https://srtm.csi.cgiar.org/srtmdata/>). The Lancang–Mekong River and watershed data are from the HydroSHEDS

database (https://data.hydrosheds.org/file/hydrosheds-v1-archive/SHP/bas_30s_shp/as_bas_30s_beta.zip). Projected FloodRI changes by the mid-twenty-first century, generated by this study⁸⁸, are available at <https://doi.org/10.5281/zenodo.13318626>.

Code availability

All analyses were performed using functions in MATLAB. The key portions of the computer code used to process the results and develop the figures⁸⁹ are available at <https://doi.org/10.5281/zenodo.13318603>.

Received: 31 May 2024; Accepted: 31 October 2024;

Published online: 14 November 2024

References

- Hu, P., Zhang, Q., Shi, P., Chen, B. & Fang, J. Flood-induced mortality across the globe: spatiotemporal pattern and influencing factors. *Sci. Total Environ.* **643**, 171–182 (2018).
- Jonkman, S. N. Global perspectives on loss of human life caused by floods. *Nat. Hazards* **34**, 151–175 (2005).
- Kundzewicz, Z. W. et al. Flood risk and climate change: global and regional perspectives. *Hydrol. Sci. J.* **59**, 1–28 (2012).
- Lai, Y. et al. Greater flood risks in response to slowdown of tropical cyclones over the coast of China. *Proc. Natl. Acad. Sci. USA* **117**, 14751–14755 (2020).
- Zhu, L. & Quiring, S. M. Exposure to precipitation from tropical cyclones has increased over the continental United States from 1948 to 2019. *Commun. Earth Environ.* **3**, <https://doi.org/10.1038/s43247-022-00639-8> (2022).
- Marsooli, R., Lin, N., Emanuel, K. & Feng, K. Climate change exacerbates hurricane flood hazards along US Atlantic and Gulf Coasts in spatially varying patterns. *Nat. Commun.* **10**, 3785 (2019).
- Gori, A., Lin, N., Xi, D. & Emanuel, K. Tropical cyclone climatology change greatly exacerbates US extreme rainfall–surge hazard. *Nat. Clim. Change* **12**, 171–178 (2022).
- Li, X. et al. Impacts of urbanization, antecedent rainfall event, and cyclone tracks on extreme floods at Houston reservoirs during Hurricane Harvey. *Environ. Res. Lett.* **15**, <https://doi.org/10.1088/1748-9326/abc4ff> (2020).
- Yang, L. et al. Riverine flooding and landfalling tropical cyclones over China. *Earth's Future* **8**, e2019EF001451 (2020).
- Zhang, W., Villarini, G., Vecchi, G. A. & Smith, J. A. Urbanization exacerbated the rainfall and flooding caused by hurricane Harvey in Houston. *Nature* **563**, 384–388 (2018).
- Jongman, B., Ward, P. J. & Aerts, J. C. J. H. Global exposure to river and coastal flooding: long term trends and changes. *Glob. Environ. Change* **22**, 823–835 (2012).
- Scott, D. T., Gomez-Velez, J. D., Jones, C. N. & Harvey, J. W. Floodplain inundation spectrum across the United States. *Nat. Commun.* **10**, 5194 (2019).
- Schumann, G. J. P. et al. Rethinking flood hazard at the global scale. *Geophys. Res. Lett.* **43**, 10, 249–10, 256 (2016).
- Yuen, K. W., Switzer, A. D., Teng, P. P. S. & Lee, J. S. H. Assessing the impacts of tropical cyclones on rice production in Bangladesh, Myanmar, Philippines, and Vietnam. *Nat. Hazards Earth Syst. Sci.* <https://doi.org/10.5194/nhess-2022-4> (2022).
- Andreadis, K. M. et al. Urbanizing the floodplain: global changes of imperviousness in flood-prone areas. *Environ. Res. Lett.* **17**, <https://doi.org/10.1088/1748-9326/ac919> (2022).
- Di Baldassarre, G. et al. Flood fatalities in Africa: from diagnosis to mitigation. *Geophys. Res. Lett.* **37** <https://doi.org/10.1029/2010gl045467> (2010)
- Güneralp, B., Güneralp, I. & Liu, Y. Changing global patterns of urban exposure to flood and drought hazards. *Glob. Environ. Change* **31**, 217–225 (2015).

18. Mazzoleni, M. et al. Floodplains in the Anthropocene: a global analysis of the interplay between human population, built environment, and flood severity. *Water Res.* **57**, <https://doi.org/10.1029/2020wr027744> (2021)
19. Neumayer, E. & Barthel, F. Normalizing economic loss from natural disasters: a global analysis. *Glob. Environ. Change* **21**, 13–24 (2011).
20. Rentschler, J., Salhab, M. & Jafino, B. A. Flood exposure and poverty in 188 countries. *Nat. Commun.* **13**, 3527 (2022).
21. Szabo, S. et al. Population dynamics, delta vulnerability and environmental change: comparison of the Mekong, Ganges-Brahmaputra and Amazon delta regions. *Sustain. Sci.* **11**, 539–554 (2016).
22. de Sherbinin, A. et al. Migration and risk: net migration in marginal ecosystems and hazardous areas. *Environ. Res. Lett.* **7** <https://doi.org/10.1088/1748-9326/7/4/045602> (2012)
23. Murakami, H. et al. Detected climatic change in global distribution of tropical cyclones. *Proc. Natl Acad. Sci. USA* **117**, 10706–10714 (2020).
24. Smith, A. et al. New estimates of flood exposure in developing countries using high-resolution population data. *Nat. Commun.* **10**, 1814 (2019).
25. Tellman, B. et al. Satellite imaging reveals increased proportion of population exposed to floods. *Nature* **596**, 80–86 (2021).
26. Park, D.-S. R., Ho, C.-H. & Kim, J.-H. Growing threat of intense tropical cyclones to East Asia over the period 1977–2010. *Environ. Res. Lett.* **9**, 014008 (2014).
27. Feng, X., Klingaman, N. P. & Hodges, K. I. Poleward migration of western North Pacific tropical cyclones related to changes in cyclone seasonality. *Nat. Commun.* **12**, 6210 (2021).
28. Chen, A. et al. An analysis of the spatial variation of tropical cyclone rainfall trends in Mainland Southeast Asia. *Int. J. Climatol.* **43**, 5912–5926 (2023).
29. Ali, H., Fowler, H. J., Vanniere, B. & Roberts, M. J. Fewer, but more intense, future tropical storms over the ganges and Mekong Basins. *Geophys. Res. Lett.* **50** <https://doi.org/10.1029/2023gl104973> (2023)
30. Chen, A., Emanuel, K. A., Chen, D., Lin, C. & Zhang, F. Rising future tropical cyclone-induced extreme winds in the Mekong River Basin. *Sci. Bull.* **65**, 419–424 (2020).
31. Winsemius, H. C. et al. Global drivers of future river flood risk. *Nat. Clim. Change* **6**, 381–385 (2015).
32. Hirabayashi, Y. et al. Global flood risk under climate change. *Nat. Clim. Change* **3**, 816–821 (2013).
33. Hoang, L. P. et al. Mekong River flow and hydrological extremes under climate change. *Hydrol. Earth Syst. Sci.* **20**, 3027–3041 (2016).
34. Huong, H. T. L. & Pathirana, A. Urbanization and climate change impacts on future urban flooding in Can Tho city, Vietnam. *Hydrol. Earth Syst. Sci.* **17**, 379–394 (2013).
35. Liang, X., Lettenmaier, D. P., Wood, E. F. & Burges, S. J. A simple hydrologically based model of land surface water and energy fluxes for general circulation models. *J. Geophys. Res.* **99**, 14415–14428 (1994).
36. Knapp, K. R., Kruk, M. C., Levinson, D. H., Diamond, H. J. & Neumann, C. J. The international best track archive for climate stewardship (IBTrACS). *Bull. Am. Meteorol. Soc.* **91**, 363–376 (2010).
37. Yamazaki, D., Kanae, S., Kim, H. & Oki, T. A physically based description of floodplain inundation dynamics in a global river routing model. *Water Res. Res.* **47**, <https://doi.org/10.1029/2010wr009726> (2011)
38. Roberts, M. J. et al. Projected future changes in tropical cyclones using the CMIP6 HighResMIP multimodel ensemble. *Geophys. Res. Lett.* **47**, e2020GL088662 (2020).
39. Bowman, A. W. & Azzalini, A. Applied smoothing techniques for data analysis. (Oxford University Press, 1997).
40. Chen, A., Ho, C.-H., Chen, D. & Azorin-Molina, C. Tropical cyclone rainfall in the Mekong River Basin for 1983–2016. *Atmos. Res.* **226**, 66–75 (2019).
41. Peduzzi, P., Dao, H., Herold, C. & Mouton, F. Assessing global exposure and vulnerability towards natural hazards: the Disaster Risk Index. *Nat. Hazards Earth Syst. Sci.* **9**, 1149–1159 (2009).
42. Edmonds, D. A., Caldwell, R. L., Brondizio, E. S. & Siani, S. M. O. Coastal flooding will disproportionately impact people on river deltas. *Nat. Commun.* **11**, 4741 (2020).
43. Peduzzi, P. et al. Global trends in tropical cyclone risk. *Nat. Clim. Change* **2**, 289–294 (2012).
44. Hauer, M. E. et al. Assessing population exposure to coastal flooding due to sea level rise. *Nat. Commun.* **12**, 6900 (2021).
45. Kossin, J. P., Emanuel, K. A. & Vecchi, G. A. The poleward migration of the location of tropical cyclone maximum intensity. *Nature* **509**, 349–352 (2014).
46. Sharmila, S. & Walsh, K. J. E. Recent poleward shift of tropical cyclone formation linked to Hadley cell expansion. *Nat. Clim. Change* **8**, 730–736 (2018).
47. Li, R. C. Y. & Zhou, W. Revisiting the intraseasonal, interannual and interdecadal variability of tropical cyclones in the western North Pacific. *Atmos. Ocean. Sci. Lett.* **11**, 198–208 (2018).
48. Knutson, T. et al. Tropical cyclones and climate change assessment: part II: projected response to anthropogenic warming. *Bull. Am. Meteorol. Soc.* **101**, E303–E322 (2020).
49. Sobel, A. H. et al. Tropical cyclone frequency. *Earth's Future* <https://doi.org/10.1029/2021ef002275> (2021)
50. Bangalore, M., Smith, A. & Veldkamp, T. Exposure to floods, climate change, and poverty in Vietnam. *Econ. Disasters Clim. Change* **3**, 79–99 (2018).
51. Ziegler, A. D., Lim, H. S., Wasson, R. J. & Williamson, F. C. Flood mortality in SE Asia: can palaeo-historical information help save lives? *Hydrol. Process.* **35**, e13989 (2020).
52. Ceola, S., Laio, F. & Montanari, A. Satellite nighttime lights reveal increasing human exposure to floods worldwide. *Geophys. Res. Lett.* **41**, 7184–7190 (2014).
53. Neumann, B., Vafeidis, A. T., Zimmermann, J. & Nicholls, R. J. Future coastal population growth and exposure to sea-level rise and coastal flooding—a global assessment. *PLoS One* **10**, e0118571 (2015).
54. Vousdoukas, M. I. et al. Global probabilistic projections of extreme sea levels show intensification of coastal flood hazard. *Nat. Commun.* **9**, 2360 (2018).
55. Erban, L. E., Gorelick, S. M. & Zebker, H. A. Groundwater extraction, land subsidence, and sea-level rise in the Mekong Delta, Vietnam. *Environ. Res. Lett.* **9**, 084010 (2014).
56. Minderhoud, P. S. J., Coumou, L., Erkens, G., Middelkoop, H. & Stouthamer, E. Mekong delta much lower than previously assumed in sea-level rise impact assessments. *Nat. Commun.* **10**, 3847 (2019).
57. Hallegatte, S. et al. Shock waves: managing the impact of climate change on poverty. (World Bank, 2016).
58. Wang, D., Scussolini, P. & Du, S. Assessing Chinese flood protection and its social divergence. *Nat. Hazards Earth Syst. Sci.* **21**, 743–755 (2021).
59. Chen, A., Giese, M. & Chen, D. Flood impact on Mainland Southeast Asia between 1985 and 2018—the role of tropical cyclones. *J. Flood Risk Manag.* **13**, e12598 (2020).
60. Seto, K. C., Güneralp, B. & Hutyra, L. R. Global forecasts of urban expansion to 2030 and direct impacts on biodiversity and carbon pools. *Proc. Natl Acad. Sci. USA* **109**, 16083–16088 (2012).
61. Sanders, B. F. et al. Large and inequitable flood risks in Los Angeles, California. *Nat. Sustain.* **6**, 47–57 (2022).
62. Wing, O. E. J. et al. Inequitable patterns of US flood risk in the Anthropocene. *Nat. Clim. Change* **12**, 156–162 (2022).

63. Mård, J., Di Baldassarre, G. & Mazzoleni, M. Nighttime light data reveal how flood protection shapes human proximity to rivers. *Sci. Adv.* **4**, eaar5779 (2018).
64. Kreibich, H. et al. The challenge of unprecedented floods and droughts in risk management. *Nature* **608**, 80–86 (2022).
65. Mohammed, I. N., Bolten, J. D., Srinivasan, R. & Lakshmi, V. Satellite observations and modeling to understand the Lower Mekong River basin streamflow variability. *J. Hydrol.* **564**, 559–573 (2018).
66. Henck, A. C., Huntington, K. W., Stone, J. O., Montgomery, D. R. & Hallet, B. Spatial controls on erosion in the three rivers region, southeastern Tibet and southwestern China. *Earth Planet. Sci. Lett.* **303**, 71–83 (2011).
67. Yatagai, A. et al. APHRODITE: constructing a long-term daily gridded precipitation dataset for asia based on a dense network of rain gauges. *Bull. Am. Meteorol. Soc.* **93**, 1401–1415 (2012).
68. Chen, A., Chen, D. & Azorin-Molina, C. Assessing reliability of precipitation data over the Mekong River basin: a comparison of ground-based, satellite, and reanalysis datasets. *Int. J. Climatol.* **38**, 4314–4334 (2018).
69. Wu, J. & Gao, X. J. A gridded daily observation dataset over China region and comparison with the other datasets. *Chin. J. Geophys.* **56**, 1102–1111 (2013).
70. Sheffield, J., Goteti, G. & Wood, E. F. Development of a 50-year high-resolution global dataset of meteorological forcings for land surface modeling. *J. Clim.* **19**, 3087–3111 (2006).
71. Hodges, K., Cobb, A. & Vidale, P. L. How well are tropical cyclones represented in reanalysis datasets? *J. Clim.* **30**, 5243–5264 (2017).
72. Fu, Z. H., Zhan, R., Zhao, J., Yamada, Y. & Song, K. Future projections of multiple tropical cyclone events in the Northern Hemisphere in the CMIP6-HighResMIP models. *Geophys. Res. Lett.* **50**, <https://doi.org/10.1029/2023gl103064> (2023).
73. Hamman, J. J., Nijssen, B., Bohn, T. J., Gergel, D. R. & Mao, Y. The variable infiltration capacity model version 5 (VIC-5): infrastructure improvements for new applications and reproducibility. *Geosci. Model Dev.* **11**, 3481–3496 (2018).
74. Yamazaki, D., de Almeida, G. A. M. & Bates, P. D. Improving computational efficiency in global river models by implementing the local inertial flow equation and a vector-based river network map. *Water Resour. Res.* **49**, 7221–7235 (2013).
75. Wang, J. et al. Modeling daily floods in the Lancang-Mekong river basin using an improved hydrological-hydrodynamic model. *Water Resour. Res.* **57**, e2021WR029734 (2021).
76. Wang, J. et al. Flood inundation in the Lancang-Mekong river basin: assessing the role of summer monsoon. *J. Hydrol.* **612** <https://doi.org/10.1016/j.jhydrol.2022.128075> (2022).
77. Peng, H., Fok, H. S., Gong, J. & Wang, L. Improving stage–discharge relation in the mekong river estuary by remotely sensed long-period ocean tides. *Rem. Sens.* **12** <https://doi.org/10.3390/rs12213648> (2020).
78. Park, E. et al. Dramatic decrease of flood frequency in the Mekong Delta due to river-bed mining and dyke construction. *Sci. Total Environ.* **723**, 138066 (2020).
79. Jiang, H. & Zipser, E. J. Contribution of tropical cyclones to the global precipitation from eight seasons of TRMM data: regional, seasonal, and interannual variations. *J. Clim.* **23**, 1526–1543 (2010).
80. Cannon, A. J., Sobie, S. R. & Murdock, T. Q. Bias correction of GCM precipitation by quantile mapping: how well do methods preserve changes in quantiles and extremes? *J. Clim.* **28**, 6938–6959 (2015).
81. Qin, X. & Dai, C. Comparison of different quantile delta mapping schemes in frequency analysis of precipitation extremes over mainland Southeast Asia under climate change. *J. Hydrol.* **606** <https://doi.org/10.1016/j.jhydrol.2021.127421> (2022).
82. Sen, P. K. Estimates of the regression coefficient based on Kendall's Tau. *J. Am. Stat. Assoc.* **63**, 1379–1389 (1968).
83. Kendall, M. G. A new measure of rank correlation. *Biometrika* **30** <https://doi.org/10.2307/2332226> (1938).
84. Nguyen, V. D., Metin, A. D., Alfieri, L., Vorogushyn, S. & Merz, B. Biases in national and continental flood risk assessments by ignoring spatial dependence. *Sci. Rep.* **10**, 19387 (2020).
85. Ward, P. J. et al. Assessing flood risk at the global scale: model setup, results, and sensitivity. *Environ. Res. Lett.* **8** <https://doi.org/10.1088/1748-9326/8/4/044019> (2013).
86. Studholme, J., Fedorov, A. V., Gulev, S. K., Emanuel, K. & Hodges, K. Poleward expansion of tropical cyclone latitudes in warming climates. *Nat. Geosci.* **15**, 14–28 (2022).
87. Chen, X., Guo, Y.-P., Tan, Z.-M. & Zhao, J. Influence of different types of ENSO events on the tropical cyclone rainfall over the western North Pacific. *Clim. Dyn.* <https://doi.org/10.1007/s00382-022-06547-z> (2022).
88. Chen, A. et al. Supplementary data to: Flood risk shifts due to tropical cyclones and population exposure in the Mekong region. *Zenodo* <https://doi.org/10.5281/zenodo.13318626> (2024).
89. Chen, A. & Liu, J. Supplementary code to: Flood risk shifts due to tropical cyclones and population exposure in the Mekong Region. *Zenodo* <https://doi.org/10.5281/zenodo.13318603> (2024).

Acknowledgements

This work was supported by the National Natural Science Foundation of China (Grant no. 42101041; 42361144001), Shenzhen Science and Technology Program (KCXFZ20201221173601003; KCXFZ20201221173412035; JCYJ20210324104004013), Guangdong Provincial Key Laboratory of Intelligent Disaster Prevention and Emergency Technologies for Urban Lifeline Engineering (2022) (Grant no. 2022B1212010016). It was also partly supported by the Henan Provincial Key Laboratory of Hydrosphere and Watershed Water Security. D.C. was supported by the Swedish Research Council VR (2021-02163 and 2022-06011). Y.P. acknowledges funding from the National Science Foundation (Award # 1752729).

Author contributions

A.C. designed the experiments and contributed to data analysis and the writing of the paper. A.C. wrote the first paper draft together with Y.P., J.W., and Z.D.; Y.P., D.C., H.H., Z.D., B.H., J.W., J.Li., H.W., and J.Liu contributed to discussions and interpretations of the results and edited the paper.

Competing interests

The authors declare no competing interests.

Additional information

Supplementary information The online version contains supplementary material available at <https://doi.org/10.1038/s43247-024-01868-9>.

Correspondence and requests for materials should be addressed to Junguo Liu.

Peer review information Communications Earth & Environment thanks the anonymous reviewers for their contribution to the peer review of this work. Primary Handling Editors: Heike Langenberg. A peer review file is available.

Reprints and permissions information is available at <http://www.nature.com/reprints>

Publisher's note Springer Nature remains neutral with regard to jurisdictional claims in published maps and institutional affiliations.

Open Access This article is licensed under a Creative Commons Attribution-NonCommercial-NoDerivatives 4.0 International License, which permits any non-commercial use, sharing, distribution and reproduction in any medium or format, as long as you give appropriate credit to the original author(s) and the source, provide a link to the Creative Commons licence, and indicate if you modified the licensed material. You do not have permission under this licence to share adapted material derived from this article or parts of it. The images or other third party material in this article are included in the article's Creative Commons licence, unless indicated otherwise in a credit line to the material. If material is not included in the article's Creative Commons licence and your intended use is not permitted by statutory regulation or exceeds the permitted use, you will need to obtain permission directly from the copyright holder. To view a copy of this licence, visit <http://creativecommons.org/licenses/by-nc-nd/4.0/>.

© The Author(s) 2024